
Improving Ab-Initio Cryo-EM Reconstruction with Semi-Amortized Pose Inference

Shayan Shekarforoush^{1, 2}
shayan@cs.toronto.edu

David B. Lindell^{1, 2}
lindell@cs.toronto.edu

Marcus A. Brubaker^{1, 2, 4}
mab@eecs.yorku.ca

David J. Fleet^{1, 2, 3}
fleet@cs.toronto.edu

¹University of Toronto ²Vector Institute ³Google DeepMind ⁴York University

Abstract

Cryo-Electron Microscopy (cryo-EM) is an increasingly popular experimental technique for estimating the 3D structure of macromolecular complexes such as proteins based on 2D images. These images are notoriously noisy, and the pose of the structure in each image is unknown *a priori*. Ab-initio 3D reconstruction from 2D images entails estimating the pose in addition to the structure. In this work, we propose a new approach to this problem. We first adopt a multi-head architecture as a pose encoder to infer multiple plausible poses per-image in an amortized fashion. This approach mitigates the high uncertainty in pose estimation by encouraging exploration of pose space early in reconstruction. Once uncertainty is reduced, we refine poses in an auto-decoding fashion. In particular, we initialize with the most likely pose and iteratively update it for individual images using stochastic gradient descent (SGD). Through evaluation on synthetic datasets, we demonstrate that our method is able to handle multi-modal pose distributions during the amortized inference stage, while the later, more flexible stage of direct pose optimization yields faster and more accurate convergence of poses compared to baselines. Finally, on experimental data, we show that our approach is faster than state-of-the-art cryoAI and achieves higher-resolution reconstruction.

1 Introduction

Single particle cryo-EM has gained popularity among structural biologists as a powerful experimental method for determining the 3D structure of macromolecular complexes, such as proteins and viruses, a key to unlocking our understanding of biological function at the scale of the cell. Thanks to pioneering advances in hardware and data processing techniques, cryo-EM has enabled reconstruction of challenging structures at atomic or near-atomic resolution [1]. During a cryo-EM experiment, a *particle stack* of $10^{4\text{--}7}$ images of a target bio-molecule are acquired using an electron microscope, from which the goal is to reconstruct the unknown 3D density map [2].

This *ab-initio* reconstruction task presents some challenges. First, the pose (i.e., orientation and position) of the particle in each observation is unknown, thus the pose must be estimated for each image. Second, the images have a low signal-to-noise ratio (SNR) to avoid electron damage during imaging (e.g., see as shown in Fig. 1). The low SNR obscures high-resolution image detail, hindering pose and structure estimation. Third, bio-molecules are typically non-rigid and exhibit structural variations within a sample. Hence, for such heterogeneous datasets, it is crucial to account for the conformational variability in order to obtain high-resolution reconstruction [3–6].

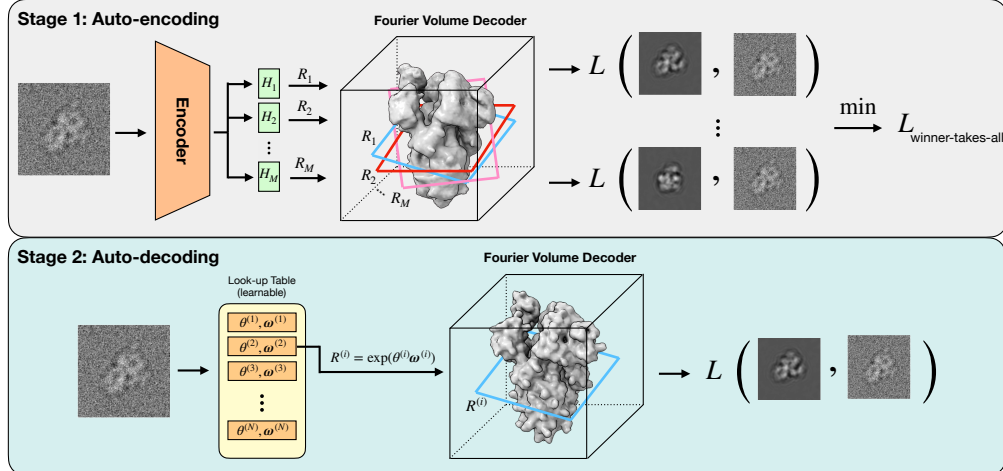


Figure 1: Our method for ab-initio reconstruction consists of two stages: (i) an auto-encoding stage where an image encoder equipped with multiple heads maps the input image to the pose candidate set $\{R_1, \dots, R_M\}$, followed by computing projections by slicing through the volume decoder in Fourier space based on the pose set. These projections are compared with the input image and the one with the minimum error is used. (ii) An auto-decoding stage where pose parameters in axis-angle representation are stored for all images. The same volume decoder is used to obtain projections, and the reconstruction loss is computed for a single projection.

Recent state of the art methods development in cryo-EM have focused on deep learning. CryoDRGN [5] proposed an image encoder-volume decoder architecture to model continuous heterogeneity, but the poses were assumed to be given. CryoDRGNv2 [7] introduced hierarchical pose search, comprising grid search followed by a form of branch-and-bound (BnB) optimization, akin to cryoSPARC [8]. More recently, cryoPoseNet [9] and cryoAI [10] introduce amortization to pose inference, to avoid the expense of orientation matching for each image. They employ a convolutional neural network (CNN) to map an input image to a pose estimate. While more efficient, amortized inference could fail to represent multi-modal posterior pose distributions that usually occur early in reconstruction. As such, compared to previous methods like cryoSPARC [8] and cryoDRGNv2 [7] that consider many pose candidates, amortized methods sometimes fail to identify the correct mode. Moreover, amortization confines the pose search to a global parametric function (the encoder) which can lead to slow convergence of poses.

Here, we introduce a new approach to ab-initio homogeneous reconstruction that is able to handle multi-modal pose distributions with a tailored encoder, and accelerates pose optimization with semi-amortization [11]. First, we perform amortized pose inference through a shared multi-choice encoder that maps each input image to multiple pose estimates (Fig. 1, top). In contrast to cryoPoseNet [9] and cryoAI [10], which use pose encoders that produce one or two estimates, we attach multiple pose predictor heads to a shared CNN feature extractor to predict multiple plausible poses for each image. By design, our multi-output encoder is able to account for pose uncertainty and encourage exploration of pose space during initial stages of reconstruction. For the 3D decoder, unlike cryoDRGN and cryoAI which use MLPs with computationally expensive feed-forward implicit networks, we adopt an explicit parameterization to further accelerate the reconstruction. To train the encoder-decoder architecture, we apply a “winner-takes-all” loss in which the 3D decoder is queried to obtain a 3D-to-2D projection for each predicted pose. Inspired by the loss function in Multi-Choice learning [12–14], we select the projection with the lowest image reconstruction error to determine the loss.

During the course of optimization, as higher resolution details are resolved, the pose posterior becomes uni-modal; thus, the pose search can be narrowed down to a neighborhood containing the most likely mode. In this stage, we propose to transition from auto-encoding to auto-decoding (Fig. 1, bottom). In particular, for each image, we choose the pose with the lowest reconstruction loss, iteratively refine it with stochastic gradient descent (SGD), and continue pose optimization and reconstruction in an alternating fashion. This direct, per-image optimization procedure achieves

faster convergence to more accurate poses than amortized inference alone, which relies on potentially sub-optimal predictions of the encoder as a parametric function.

We evaluate our approach and compare it with two state-of-the-art methods, namely, cryoSPARC [8] and cryoAI [10], on synthetic and real experimental datasets. Using synthetic data, we validate that semi-amortized inference noticeably accelerates the convergence of poses and yields reconstructions at similar or higher resolutions. We also show that our multi-choice encoder empirically accounts for multiple modes in the pose posterior. Finally, we apply our method to an experimental dataset and obtain reconstruction outperforming cryoAI and competitive with cryoSPARC.

To summarize, we make following contributions.

- Building upon cryoAI, we develop a new encoder based on a multi-head architecture to return multiple plausible candidates to further mitigate pose ambiguity.
- We train the encoder coupled with an explicit volume decoder using a “winner-takes-all” loss that penalizes the pose hypothesis with least reconstruction error.
- We introduce semi-amortization to pose inference which begins with amortized pose estimation by an encoder, followed by direct pose optimization for individual images.
- In ab-initio reconstruction, our semi-amortized method is faster than amortized method of cryoAI and achieves higher-resolution on synthetic and experimental datasets.

2 Related work

Cryo-EM reconstruction. Methods for cryo-EM reconstruction can be categorized as either homogeneous or heterogeneous. Homogeneous techniques [8–10] assume a rigid structure while heterogeneous ones [5, 7, 6, 15] allow for conformational variation. We focus on homogeneous reconstruction, but our optimization framework could be extended to heterogeneous data as well.

Conventional homogeneous reconstruction techniques rely on common-lines [16–18] or projection mapping [19, 20] to select optimal poses. Other works [21, 22] frame the reconstruction problem in the context of maximum a posteriori (MAP) estimation, and jointly reconstructs poses and structure via expectation maximization (EM). We compare our approach to cryoSPARC [8], a state-of-the-art method that uses stochastic gradient descent and a branch-and-bound search [23] for ab initio reconstruction and pose estimation. Like these methods, our auto-decoding stage directly optimizes pose of every image.

More recently, amortized inference techniques have been proposed for pose estimation [24, 9, 10, 15]. These techniques avoid explicit per-image pose optimization; instead, they train an auto-encoder or variational one [25] to associate each particle image with a predicted pose [9]. One challenge is that the auto-encoders can become stuck in local optima during training [9]. To address this issue, cryoAI [10] produces two pose estimates per image coupled with a symmetrized loss function that penalizes the best one. We build on this concept by adopting a multi-head neural architecture as the encoder to output multiple plausible pose candidates and avoid local optima.

Multi-choice learning (MCL). Inspired by scenarios where a set of hypotheses needs to be generated to account for uncertainty in the prediction task, MCL [12] was introduced in a supervised setup to learn multiple structured-outputs with SSVMs [26]. Their motivating question was: *can we learn to produce a set of plausible hypotheses?* To address this, they define an “oracle” loss in which only *the most accurate* output pays the penalty. This loss is minimized even if there is only a single accurate prediction in the set. The early follow-up work [27, 13] uses the same loss to learn a deep CNN ensemble composed of M heads with a shared backbone network. Importantly, they show that the ensemble-mean loss hurts prediction diversity across different heads, while training with the “oracle” loss yields specialized heads. Variations have since been proposed to mitigate hypothesis collapse or overconfidence issues in MCL by modifying the loss or applying learnable probabilistic scoring schemes [28–30, 14]. MCL has been used to mitigate the ambiguity in several tasks including image segmentation [31], optical-flow estimation [32], trajectory forecasting [33], human pose and shape estimation [14, 34]. In our work, we use the “oracle” loss in context of auto-encoder which supervises the pose encoder indirectly through projections provided by the decoder.

3 Problem Definition

The image formation model for cryo-EM is often well-approximated using the weak-phase object model [35]. This model assumes the 3D structure is an unknown density map, $V : \mathbb{R}^3 \rightarrow \mathbb{R}_{\geq 0}$, represented under a canonical orientation. Cryo-EM images, $\{I_i\}_{i=1}^N$, are approximated as orthographic projections of the 3D map that are oriented and shifted by unknown rotation $R_i \in SO(3)$ and in-plane translation $t_i = (t_x, t_y) \in \mathbb{R}^2$. Formally,

$$I_i(x, y) = [g_i \star (S_{t_i} \mathcal{P}_{R_i} V)](x, y) + n(x, y), \quad (1)$$

where $\mathcal{P}_{R_i}(\cdot)$ is the linear operator computing the integral along the optical axis, z , over the input density map rotated by R_i , and S is the shift operator. The projection is convolved with the image-specific point-spread function (PSF), g_i , and corrupted by additive noise n . It is common to assume that n follows a zero-mean white (or colored) Gaussian distribution.

By the Fourier slice theorem [36], the Fourier transform of a projection is equal to a central slice through the density map's 3D Fourier spectrum. Consequently,

$$\hat{I}_i(\omega_x, \omega_y) = \hat{g}_i \hat{S}_{t_i} (\hat{\mathcal{P}}_{R_i} \hat{V})(\omega_x, \omega_y) + \hat{n}(\omega_x, \omega_y), \quad (2)$$

where \hat{I} and \hat{V} denote the 2D and 3D Fourier transforms of the image and the density map. The slice perpendicular to the projection is computed by $(\hat{\mathcal{P}}_{R_i} \hat{V})$. The translation by S_{t_i} becomes a phase shift operator \hat{S}_{t_i} , and convolution with g_i is equivalent to element-wise multiplication with, \hat{g}_i , the contrast transfer function (CTF). The noise \hat{n} remains zero-mean Gaussian.

Under this model, given the structure \hat{V} , the negative log-likelihood of observing image \hat{I}_i with noise variance σ^2 and poses (R_i, t_i) is

$$\mathcal{L} = -\frac{1}{2\sigma^2} \sum_{\omega_x, \omega_y} [\hat{g}_i \hat{S}_{t_i} (\hat{\mathcal{P}}_{R_i} \hat{V})(\omega_x, \omega_y) - \hat{I}_i(\omega_x, \omega_y)]^2. \quad (3)$$

Ab-initio reconstruction methods [8–10, 7] solve jointly for the unknown structure \hat{V} and poses (R_i, t_i) . They often follow an Expectation-Maximization (EM) [37, 21] procedure in which the E-step aligns images with the structure yielding pose estimates (R_i, t_i) , and then in the M-step the volume \hat{V} is updated by minimizing the negative log-likelihood in Eq. 3. Since errors in pose estimates lead to blurry reconstructions, accurate pose estimates are crucial to finding high-resolution structures. As discussed above, poses are either optimized through search and projection matching [8, 7] or estimated by an encoder network [10, 9, 15].

4 Methodology

We propose a two-staged approach to ab-initio cryo-EM reconstruction by mixing auto-encoding and auto-decoding. In particular, we start with amortized inference (Fig. 1, auto-encoding) where a shared encoder, equipped with multiple heads, outputs a set of pose guesses. Once the pose posterior becomes less uncertain, we switch to direct pose optimization (Fig. 1, auto-decoding). The former enables handling the pose uncertainty early in reconstruction while the latter circumvents sub-optimality of encoder network leading to arguably more accurate poses and faster convergence. We couple our pose estimation module with an explicit volumetric decoder representing the 3D structure in Hartley space [5]. Our explicit model enables faster evaluation of projections compared to multiple passes through implicit neural representations [38–40]. The following sections discuss these components in detail.

4.1 Multi-choice encoder

With randomly initialized or a low-resolution reconstruction, the pose posterior contains multiple modes. Also, due to high levels of noise in images and near-symmetries in biological structures, pose estimation inherently involves high uncertainty. As a result, there exist several equally-plausible poses for each image, and naive optimization or search is prone to local minima.

To account for uncertainty in pose estimation, we build upon cryoAI [10] and extend the encoder to return multiple rotations as candidate poses. Formally, given the i -th image, $I_i \in \mathbb{R}^{H \times W}$, multiple

rotations are computed as,

$$F_i = \text{VGG}(I_i) \quad (4)$$

$$R_{i,j} = H_{\theta_j}(F_i), \quad 1 \leq j \leq M \quad (5)$$

where a shared convolutional backbone based on the VGG16 architecture [41] extracts image-specific intermediate features, $F_i \in \mathbb{R}^{C \times H \times W}$. These features are then supplied to M separate pose predictor heads, $H_{\theta_j}, 1 \leq j \leq M$, yielding the pose set $\{R_{i,1}, \dots, R_{i,M}\}$. Heads are composed of fully-connected layers with distinct learnable weights, while the backbone is shared across all heads. Using multiple heads facilitates pose exploration and reduces uncertainty in the pose estimation process. Moreover, as θ_j are randomly initialized, different heads are free to specialize on subsets of pose space so that they collectively produce a set of likely poses $\{R_{i,1}, \dots, R_{i,M}\}$. In practice, we find that different heads specialize to non-overlapping regions of $SO(3)$ space (see Supp. B) and are thus complementary for accurate pose estimation across the entire dataset.

Inspired by multi-choice learning [12–14], we optimize the encoder-decoder using a “winner-takes-all” loss. For each image I_i and predicted pose $R_{i,j}$, the negative log-likelihood, $\mathcal{L}_{i,j}$ in (Eq. 3), is computed, and the minimum is selected as the final loss for the corresponding image, i.e.,

$$\mathcal{L}_i = \min_j \mathcal{L}_{i,j}. \quad (6)$$

Minimizing this loss requires only one of the predicted poses to be accurate. CryoAI [10] can be viewed a special case of this formulation; it assigns two poses to each image as a consequence of input augmentation, and selects the best one with a symmetrized loss. In contrast, our approach augments the output of the encoder network with multiple heads, each providing a pose estimate.

4.2 Switching from auto-encoding to auto-decoding

Unlike in early stages when high uncertainty encourages pose exploration, in later stages, as higher frequency details of the structure are resolved, the true pose posterior becomes more concentrated about a single mode. At this point, the gap between the predicted and true posteriors is mainly determined by the error in the pose estimate (predicted mean), prioritizing accuracy over exploration. However, pose inference by a feed-forward network, as a parametric function of the input image, may produce estimates with substantial error, rendering amortization as a barrier to further refinement of the 3D structure. In prior work [11, 42–44], a similar issue called the *amortization gap* has been discussed which measures the KL-divergence between the true and predicted variational posteriors.

To address this issue, we adopt a semi-amortized inference scheme [11] comprising two stages. First, the encoder predicts a set of pose candidates using a multi-head architecture. In the second stage, rather than amortized inference, pose parameters are directly optimized for each image using stochastic gradient descent. To initialize poses for the i -th image, we choose the one with the lowest reconstruction loss from the set of candidates $\{R_{i,1}, \dots, R_{i,M}\}$, namely $R_i^* = R_{i,s}$ such that

$$s = \arg \min_i \mathcal{L}_i. \quad (7)$$

Subsequently, the pose and structure are optimized by coordinate descent using the negative log-likelihood (Eq. 3) as the objective function. Please see Supp. A for more details on pose optimization.

4.3 Explicit representation as volume decoder

Recent works [10, 5] use coordinate networks [39, 40, 38] to implicitly model the Fourier representation of the 3D structure. Instead, we couple the pose estimation module with an explicit parameterization of the structure in the Fourier domain. The explicit representation is less computationally expensive than an MLP to evaluate and update. Also, this choice is motivated by the fact the implicit decoder needs to be queried multiple times for each image with the multi-head encoder.

We parameterize the volume using the Hartley representation [5]. The Fourier and Hartley transforms, respectively denoted as $F(\omega)$ and $H(\omega)$, are related as

$$H(\omega) = \mathcal{R}[F(\omega)] - i\mathcal{I}[F(\omega)], \quad (8)$$

where ω denotes the frequency coordinate and \mathcal{R} and \mathcal{I} are the real and imaginary part, respectively. The Hartley representation is real-valued, and so more memory efficient to use than storing complex-valued Fourier coefficients. To account for high dynamic range of the Hartley coefficients, we assume the Hartley field is decomposed into mantissa, $m(\omega)$ and exponent $e(\omega)$ fields [10] as,

$$H(\omega) = m(\omega) \times \exp(e(\omega)). \quad (9)$$

This decomposition restricts the range of values for $m(\omega)$ and $e(\omega)$ and makes the reconstruction less sensitive to the initialization of the field.

5 Experiments

We use both synthetic and real datasets to compare our semi-amortized ab-initio reconstruction method with state-of-the-art methods, cryoAI [10] that uses amortized inference for the entire reconstruction, and cryoSPARC [8] that performs pose search separately for each image.

Synthetic data. We generate synthetic datasets by simulating the image formation process formalized in Sec. 3 using atomic models deposited in the Protein Data Bank (PDB). We compute ground-truth density maps of size 128^3 for a heat shock protein (HSP) [45] (1.5 \AA), pre-catalytic spliceosome [46] (4.33 \AA), and SARS-CoV-2 spike protein [47] (2.13 \AA). Then, $N = 50,000$ projections of size $L = 128$ are generated by randomly rotating and projecting the density map along the canonical z-axis. Finally, a random CTF is applied in the Fourier space and Gaussian noise is added yielding SNR = 0.1.

Experimental data. We use the 80S experimental dataset EMPIAR-10028 [48] containing 105,247 images of length $L = 360$ with pixel size 1.34 \AA . We downsample the images to $L = 128$ (3.76 \AA) using cryoSPARC software [8], and randomly split the data into two halves and run the reconstruction methods independently on each. In our method, we make the assumption that particles are centered in the image box, while cryoAI is able to estimate the in-plane translation using a separate encoder. To ensure fair comparison, we use translation parameters estimated by cryoSPARC software and preprocess images to shift particles to the center. To be consistent, we use the same data with cryoAI and disable translation estimation.

Implementation details. During auto-encoding, we use encoders with $M = 7$ and $M = 15$ heads for reconstruction on synthetic and real datasets, respectively, with Adam [49] to optimize encoder and decoder with learning rates 0.0001 and 0.05. Once switched to direct optimization (after 7 epochs for synthetic and 15 epochs for real data), we reduce the decoder learning rate to 0.02 and allocate a new optimizer for pose parameters with learning rate 0.05. To be consistent with cryoAI, we use a batch size of 64 and train for the same number of epochs (20 for synthetic and 30 for real data). We use the public cryoAI codebase and run cryoSPARC v4.4.0 [8] with default settings. Methods are implemented in Pytorch [50]. Experiment are run on a single NVIDIA A40 GPU.

5.1 Results

We first qualitatively compare final reconstructions of our semi-amortized approach with cryoAI [10] and cryoSPARC [8] on synthetic and real datasets (Fig. 2, left). Both our method and cryoSPARC capture high-frequency details of the 3D structure on all datasets, whereas reconstructions obtained by cryoAI on the HSP and 80S datasets are inferior. In particular, on HSP, cryoAI gets stuck in local minima as it fails to handle high uncertainty in poses caused by symmetries in this structure.

For quantitative comparison, we visualize the Fourier Shell Correlation (FSC) [52] between the reconstruction and the ground truth (Fig. 2, right). FSC is the gold-standard metric measuring the normalised cross-correlation coefficient between two 3D Fourier volumes along shells of increasing radius. Higher FSC implies more accurate reconstruction. On the Spliceosome, HSP and 80S experimental datasets, our reconstruction outperforms cryoAI. Also, our method outperforms cryoSPARC on Spliceosome and HSP while achieving competitive FSC on Spike and 80S. We use the standard 0.5 and 0.143 cutoff thresholds to report the resolution for synthetic and real data, respectively. Our method achieves higher or competitive resolution compared to cryoAI and cryoSPARC on all datasets.

In Fig. 3, we visualize resolution-time plots, showing that our semi-amortized method gets to high-resolution reconstructions significantly faster than cryoAI. In fact, semi-amortization accelerates the improvement in the resolution and with our explicit structure decoder, we circumvent expensive

Table 1: Pose accuracy quantified as mean/median errors in units of degrees evaluated on synthetic datasets.

Method	HSP	Spike	Spliceosome
CryoSPARC [8]	6.23 / 1.05	1.61 / 1.51	1.41 / 1.36
CryoAI [10]	45.83 / 61.86	2.52 / 2.29	2.85 / 2.61
Ours	3.27 / 0.97	1.54 / 0.90	0.68 / 0.61

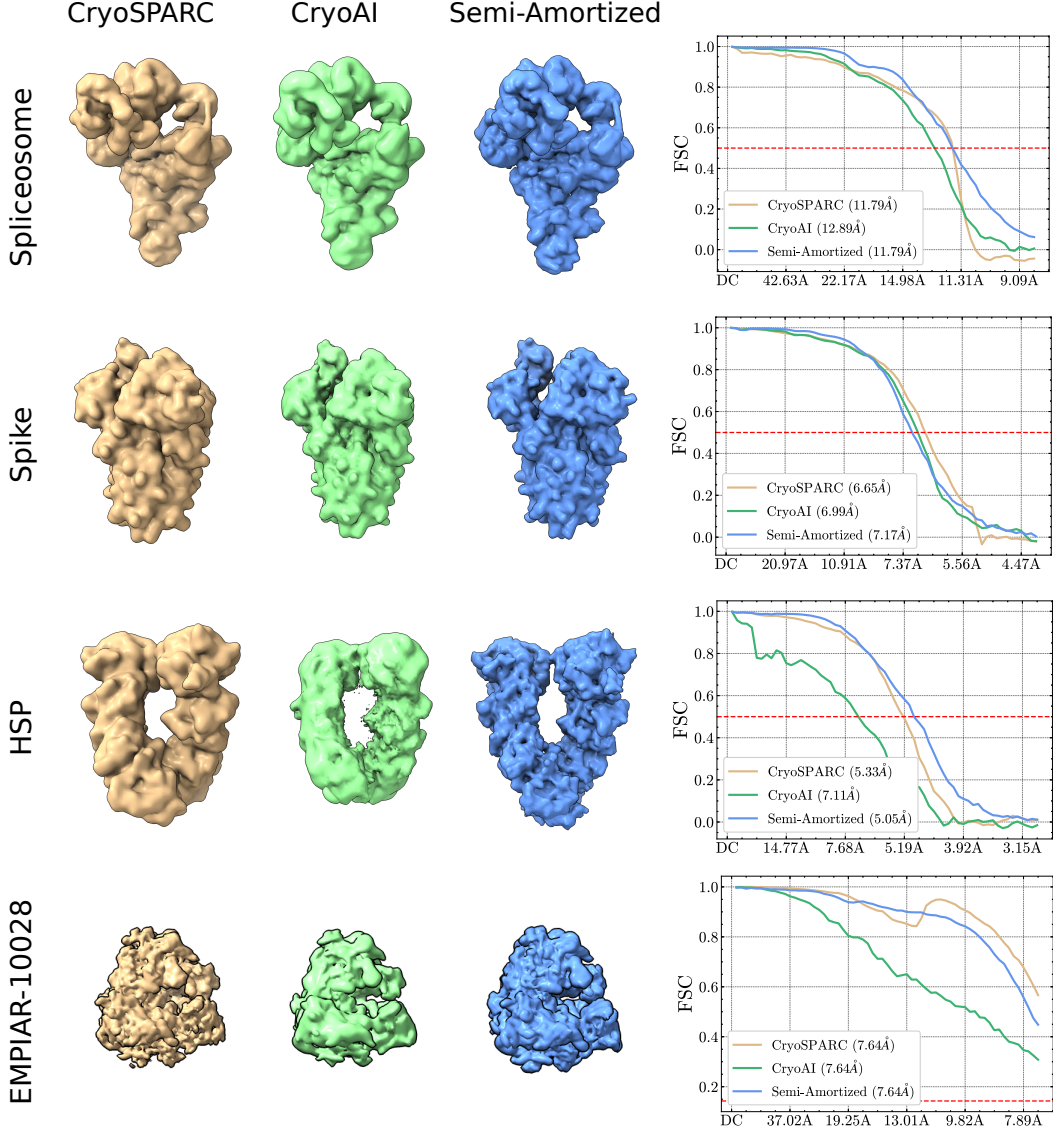


Figure 2: Qualitative and quantitative comparison of reconstructions obtained by our proposed semi-amortized method with cryoAI [10] and cryoSPARC [8]. (**Left**) Final 3D reconstructions on three synthetic datasets and one experimental dataset (EMPIAR-10028) are depicted using ChimeraX [51]. (**Right**) FSC curves are visualized for quantitative comparison. The red dashed lines show the standard threshold levels of 0.5 and 0.143 to report the resolution (in Angstrom) for synthetic and real data, respectively. Our method achieves higher resolution on the Spliceosome and HSP datasets, and it is competitive with the state of the art on the Spike and EMPIAR-10028 datasets.

MLP evaluations and train faster without any degradation to the final reconstruction quality as shown in Fig. 2. Finally, we report the mean and median errors in estimated poses on synthetic datasets in Table 1, showing that our method outperforms cryoSPARC and cryoAI. High errors by cryoAI on HSP dataset shows that it gets stuck in local minima and fails to accurately estimate poses.

5.2 Semi-Amortized vs. Fully-Amortized

To showcase the benefit of the auto-decoding stage, we compare our semi-amortized method with a fully-amortized baseline on spike and spliceosome datasets. Starting with auto-encoding, we branch the running reconstruction into two after 7 epochs: the first continues using the encoder while the second switches to direct pose optimization. We plot the average pose error with respect to the ground-truth at different epochs in Fig. 4 (left). When using the multi-head encoder, the pose with the

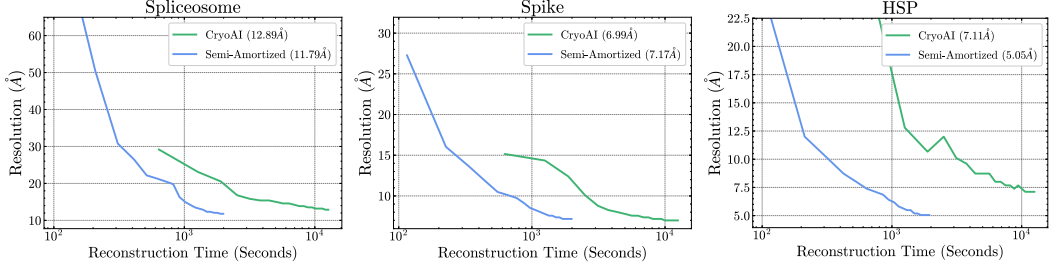


Figure 3: 3D resolution as a function of log time for different methods. These plots show the semi-amortized method is significantly faster than cryoAI.

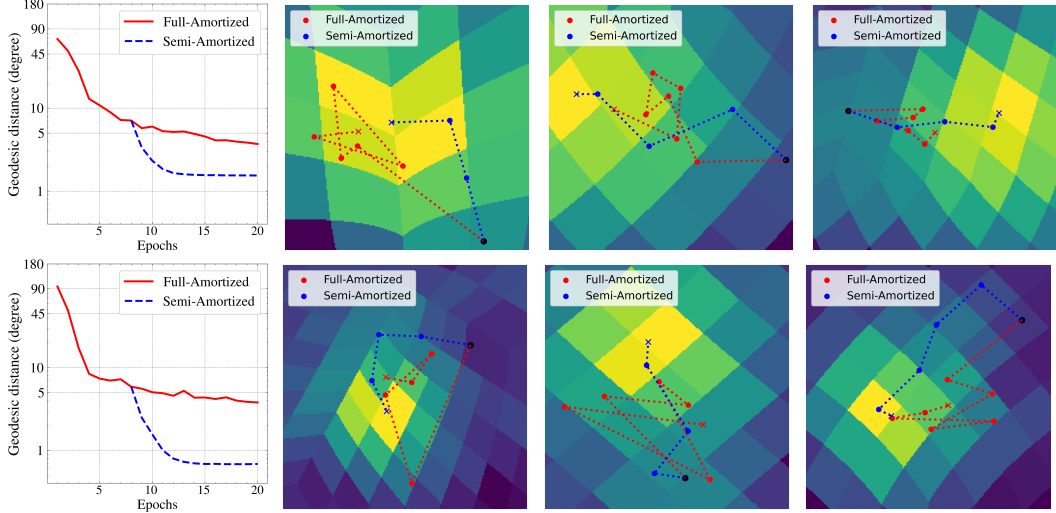


Figure 4: Quantitative and qualitative comparison of fully- vs. semi-amortized methods in pose optimization for Spliceosome and Spike datasets (two rows). (**Right**) The mean of geodesic distances between the predicted pose and ground-truth is visualized at different epochs. By switching from amortized inference to direct optimization, semi-amortized method (**blue**) enjoys accelerated pose convergence compared to fully-amortized one (**red**). (**Left**) Through some examples, the progress of pose inference methods are compared qualitatively. Each plot corresponds to the approximate log posterior for an image, marginalized over in-plane rotations, as view-direction distribution depicted over HEALPix [53] uniform grid on a unit sphere S^2 . After Gnomonic projection to 2D space, the view is limited to a neighborhood around the mode of interest. **Black** dot is the starting point while **blue** dots and **red** dots show poses estimated by fully- and semi-amortized methods, respectively.

least reconstruction error is selected among the candidates. Interestingly, as our method switches to direct pose optimization, the error in pose drops quickly, whereas the fully-amortized baseline exhibits slow convergence. This clearly shows the superiority of auto-decoding compared to auto-encoding during the later stages of optimization.

Next, we analyze the evolution of pose estimates over the optimization landscape depicted as a heat map (Fig. 4, right). Qualitatively, poses obtained by direct optimization (blue dots) show stable convergence to the optimal point (highlighted area) while those inferred by the encoder (red dots) frequently oscillate. Indeed, the encoder in amortized inference is a globally parameterized function which might be too restrictive, yielding sub-optimal pose parameters. Therefore, poses inferred in an amortized fashion might fail to consistently converge to the optimal point. On other hand, direct optimization is intuitively more flexible as it is performed separately and locally for each image, exhibiting more stable convergence. See Supp. C for more examples.

5.3 Multi-Modal Pose Posterior

Lastly, we examine how well our multi-head encoder performs vs. cryoAI encoder in terms of handling the uncertainty in the pose on the challenging dataset of HSP [45]. To simplify the visualization, we run our method with $M = 4$ heads in this experiment. We first inspect the behavior of encoders

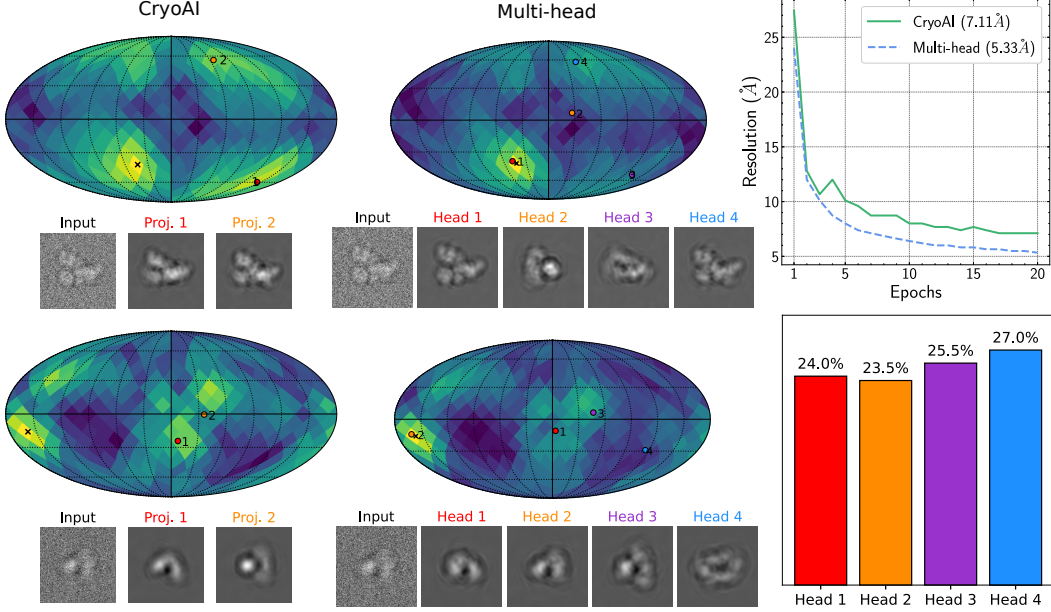


Figure 5: Comparing performance of our multi-head pose encoder ($M = 4$) with cryoAI pose encoder on the challenging HSP [45] dataset. **(Left)** The approximate log posterior of view direction is visualized on the unit sphere with highlighted areas showing modes of the distribution. CryoAI and multi-head encoders provide two and four pose estimates, respectively, which are marked with colored dots on the sphere (the order of poses is arbitrary). Below the sphere, the corresponding projections are illustrated. CryoAI fails to find the correct mode while our method is able cover multiple modes. **(Top, right)** With our multi-head encoder, the reconstruction converges to a much higher resolution compared to cryoAI. **(Bottom, right)** Percentage of images assigned to each head is visualized as a bar plot confirming that all heads participate in pose estimation.

for two example cryo-EM images (Fig. 5, left, see Supp. D for more examples). In each row, the approximate posterior distribution over view direction is visualized for both cryoAI and multi-head encoders given the input image and reconstruction. Our multi-head encoder returns a set of plausible candidates, while cryoAI obtains two pose estimates by data augmentation. In both examples, the multi-head encoder identifies the correct mode while cryoAI selects the incorrect one. Note that the pose set predicted by the multi-head encoder contains other posterior modes as well. Intuitively, cryoAI encoder with two pose predictions cannot explore the pose space as much as our multi-head encoder. Thus, the pose posterior in cryoAI remains uncertain and multi-modal during reconstruction. This also contributes to slower convergence to higher-resolution reconstructions as depicted in the top left of Fig. 5. Finally, we visualize the percentage of images assigned to each head by our “winner-takes-all” loss. The relatively even spread of assignments to different heads shows that the multi-head encoder does not suffer hypotheses collapse [30], namely all heads actively participate in the pose prediction. In Supp. B, we investigate how each head specializes in pose prediction for non-overlapping regions of $SO(3)$.

6 Conclusion, Limitations and Future Work

In this paper, we propose a new semi-amortized approach to ab initio cryo-EM reconstruction. We develop a new multi-head encoder that estimates a set of plausible candidate pose to handle the uncertainty. As the uncertainty is reduced, we transition to an auto-decoding stage where poses are iteratively optimized using SGD for each image. Our results show that our multi-head encoder is able to capture multiple modes of the pose distribution, and our flexible direct optimization enables accelerated convergence of poses and reconstructions. Our method outperforms cryoAI on experimental data and achieves competitive results with cryoSPARC.

Limitations. In this work, we assume that the 3D structure is rigid while they are often flexible and deform within the sample. Also, for simplicity, the particles are assumed to be centered in the frame.

As a promising direction for future work, our semi-amortized method with multi-head encoder can be extended to include other latent variables of translation and heterogeneity as well. Moreover, developing a well-defined heuristic to decide on relative length of two stages of auto-encoding and auto-decoding is also an interesting direction to explore in the future.

Societal Impact. Structure determination with Cryo-EM for macromolecular is one of the most exciting areas in structural biology with vast social impact. For instance, cryo-EM tools were used in recovering the structure of the SARS-COV2 spike protein, the discovery of its pre-fusion conformation, and the evaluation of potential medical treatments.

Acknowledgments and Disclosure of Funding

This research was supported in part by the Province of Ontario, the Government of Canada, through NSERC, CIFAR, and the Canada First Research Excellence Fund for the Vision: Science to Applications (VISTA) programme, and by companies sponsoring the Vector Institute.

References

- [1] Werner Kühlbrandt. The resolution revolution. *Science*, 343(6178):1443–1444, 2014.
- [2] Amit Singer and Fred J Sigworth. Computational methods for single-particle electron cryomicroscopy. *Annual Review of Biomedical Data Science*, 3:163–190, 2020.
- [3] Sjors HW Scheres, Haixiao Gao, Mikel Valle, Gabor T Herman, Paul PB Eggermont, Joachim Frank, and Jose-Maria Carazo. Disentangling conformational states of macromolecules in 3d-em through likelihood optimization. *Nature Methods*, 4(1):27–29, 2007.
- [4] Roy R Lederman, Joakim Andén, and Amit Singer. Hyper-molecules: On the representation and recovery of dynamical structures, with application to flexible macro-molecular structures in cryo-em. *arXiv preprint arXiv:1907.01589*, 2019.
- [5] Ellen D Zhong, Tristan Bepler, Bonnie Berger, and Joseph H Davis. CryoDRGN: reconstruction of heterogeneous cryo-EM structures using neural networks. *Nature Methods*, 18(2):176–185, 2021.
- [6] Ali Punjani and David J Fleet. 3DFlex: determining structure and motion of flexible proteins from cryo-EM. *Nature Methods*, pages 1–11, 2023.
- [7] Ellen D Zhong, Adam Lerer, Joseph H Davis, and Bonnie Berger. CryoDRGN2: Ab initio neural reconstruction of 3d protein structures from real cryo-EM images. In *Proceedings of the IEEE/CVF International Conference on Computer Vision*, pages 4066–4075, 2021.
- [8] Ali Punjani, John L Rubinstein, David J Fleet, and Marcus A Brubaker. cryoSPARC: algorithms for rapid unsupervised cryo-EM structure determination. *Nature Methods*, 14(3):290–296, 2017.
- [9] Youssef SG Nashed, Frédéric Poitevin, Harshit Gupta, Geoffrey Woppard, Michael Kagan, Chun Hong Yoon, and Daniel Ratner. CryoPoseNet: End-to-end simultaneous learning of single-particle orientation and 3D map reconstruction from cryo-electron microscopy data. In *Proceedings of the IEEE/CVF International Conference on Computer Vision*, pages 4066–4076, 2021.
- [10] Axel Levy, Frédéric Poitevin, Julien Martel, Youssef Nashed, Ariana Peck, Nina Miolane, Daniel Ratner, Mike Dunne, and Gordon Wetzstein. CryoAI: Amortized inference of poses for ab initio reconstruction of 3d molecular volumes from real cryo-EM images. In *European Conference on Computer Vision*, pages 540–557. Springer, 2022.
- [11] Yoon Kim, Sam Wiseman, Andrew Miller, David Sontag, and Alexander Rush. Semi-amortized variational autoencoders. In *International Conference on Machine Learning*, pages 2678–2687. PMLR, 2018.

- [12] Abner Guzman-Rivera, Dhruv Batra, and Pushmeet Kohli. Multiple choice learning: Learning to produce multiple structured outputs. *Advances in Neural Information Processing Systems*, 25, 2012.
- [13] Stefan Lee, Senthil Purushwalkam Shiva Prakash, Michael Cogswell, Viresh Ranjan, David Crandall, and Dhruv Batra. Stochastic multiple choice learning for training diverse deep ensembles. *Advances in Neural Information Processing Systems*, 29, 2016.
- [14] Christian Rupprecht, Iro Laina, Robert DiPietro, Maximilian Baust, Federico Tombari, Nassir Navab, and Gregory D Hager. Learning in an uncertain world: Representing ambiguity through multiple hypotheses. In *Proceedings of the IEEE International Conference on Computer Vision*, pages 3591–3600, 2017.
- [15] Axel Levy, Gordon Wetzstein, Julien NP Martel, Frederic Poitevin, and Ellen Zhong. Amortized inference for heterogeneous reconstruction in cryo-EM. *Advances in Neural Information Processing Systems*, 35:13038–13049, 2022.
- [16] Amit Singer, Ronald R Coifman, Fred J Sigworth, David W Chester, and Yoel Shkolnisky. Detecting consistent common lines in cryo-EM by voting. *Journal of Structural Biology*, 169(3):312–322, 2010.
- [17] Ido Greenberg and Yoel Shkolnisky. Common lines modeling for reference free ab-initio reconstruction in cryo-EM. *Journal of Structural Biology*, 200(2):106–117, 2017.
- [18] Gabi Pragier and Yoel Shkolnisky. A common lines approach for ab initio modeling of cyclically symmetric molecules. *Inverse Problems*, 35(12):124005, 2019.
- [19] Paweł A Penczek, Robert A Grassucci, and Joachim Frank. The ribosome at improved resolution: new techniques for merging and orientation refinement in 3D cryo-electron microscopy of biological particles. *Ultramicroscopy*, 53(3):251–270, 1994.
- [20] Timothy S Baker and R Holland Cheng. A model-based approach for determining orientations of biological macromolecules imaged by cryoelectron microscopy. *Journal of Structural Biology*, 116(1):120–130, 1996.
- [21] Sjors HW Scheres. A Bayesian view on cryo-EM structure determination. *Journal of Molecular Biology*, 415(2):406–418, 2012.
- [22] Sjors HW Scheres. RELION: implementation of a Bayesian approach to cryo-EM structure determination. *Journal of Structural Biology*, 180(3):519–530, 2012.
- [23] Eugene L Lawler and David E Wood. Branch-and-bound methods: A survey. *Operations Research*, 14(4):699–719, 1966.
- [24] Dan Rosenbaum, Marta Garnelo, Michal Zielinski, Charlie Beattie, Ellen Clancy, Andrea Huber, Pushmeet Kohli, Andrew W Senior, John Jumper, Carl Doersch, et al. Inferring a continuous distribution of atom coordinates from cryo-EM images using VAEs. *arXiv preprint arXiv:2106.14108*, 2021.
- [25] Diederik P Kingma and Max Welling. Auto-encoding variational bayes. *arXiv preprint arXiv:1312.6114*, 2013.
- [26] Ioannis Tschantzidis, Thorsten Joachims, Thomas Hofmann, Yasemin Altun, and Yoram Singer. Large margin methods for structured and interdependent output variables. *Journal of Machine Learning Research*, 6(9), 2005.
- [27] Stefan Lee, Senthil Purushwalkam, Michael Cogswell, David Crandall, and Dhruv Batra. Why m heads are better than one: Training a diverse ensemble of deep networks. *arXiv preprint arXiv:1511.06314*, 2015.
- [28] Kimin Lee, Changho Hwang, KyoungSoo Park, and Jinwoo Shin. Confident multiple choice learning. In *International Conference on Machine Learning*, pages 2014–2023. PMLR, 2017.

- [29] Kai Tian, Yi Xu, Shuigeng Zhou, and Jihong Guan. Versatile multiple choice learning and its application to vision computing. In *Proceedings of the IEEE/CVF Conference on Computer Vision and Pattern Recognition*, pages 6349–6357, 2019.
- [30] Victor Letzelter, Mathieu Fontaine, Mickaël Chen, Patrick Pérez, Slim Essid, and Gael Richard. Resilient multiple choice learning: A learned scoring scheme with application to audio scene analysis. *Advances in Neural Information Processing Systems*, 36, 2024.
- [31] Simon Kohl, Bernardino Romera-Paredes, Clemens Meyer, Jeffrey De Fauw, Joseph R Ledsam, Klaus Maier-Hein, SM Eslami, Danilo Jimenez Rezende, and Olaf Ronneberger. A probabilistic U-Net for segmentation of ambiguous images. *Advances in Neural Information Processing Systems*, 31, 2018.
- [32] Eddy Ilg, Ozgun Cicek, Silvio Galessio, Aaron Klein, Osama Makansi, Frank Hutter, and Thomas Brox. Uncertainty estimates and multi-hypotheses networks for optical flow. In *European Conference on Computer Vision*, pages 652–667, 2018.
- [33] Ye Yuan and Kris Kitani. Diverse trajectory forecasting with determinantal point processes. *arXiv preprint arXiv:1907.04967*, 2019.
- [34] Benjamin Biggs, David Novotny, Sébastien Ehrhardt, Hanbyul Joo, Ben Graham, and Andrea Vedaldi. 3D Multi-bodies: Fitting sets of plausible 3d human models to ambiguous image data. *Advances in Neural Information Processing Systems*, 33:20496–20507, 2020.
- [35] Earl J Kirkland. *Advanced computing in electron microscopy*, volume 12. Springer, 1998.
- [36] Ronald N Bracewell. Strip integration in radio astronomy. *Australian Journal of Physics*, 9(2):198–217, 1956.
- [37] Todd K Moon. The expectation-maximization algorithm. *IEEE Signal processing magazine*, 13(6):47–60, 1996.
- [38] Vincent Sitzmann, Julien Martel, Alexander Bergman, David Lindell, and Gordon Wetzstein. Implicit neural representations with periodic activation functions. *Advances in Neural Information Processing Systems*, 33:7462–7473, 2020.
- [39] Matthew Tancik, Pratul Srinivasan, Ben Mildenhall, Sara Fridovich-Keil, Nithin Raghavan, Utkarsh Singhal, Ravi Ramamoorthi, Jonathan Barron, and Ren Ng. Fourier features let networks learn high frequency functions in low dimensional domains. *Advances in Neural Information Processing Systems*, 33:7537–7547, 2020.
- [40] Ben Mildenhall, Pratul P Srinivasan, Matthew Tancik, Jonathan T Barron, Ravi Ramamoorthi, and Ren Ng. Nerf: Representing scenes as neural radiance fields for view synthesis. *Communications of the ACM*, 65(1):99–106, 2021.
- [41] Karen Simonyan and Andrew Zisserman. Very deep convolutional networks for large-scale image recognition. *arXiv preprint arXiv:1409.1556*, 2014.
- [42] Devon Hjelm, Russ R Salakhutdinov, Kyunghyun Cho, Nebojsa Jojic, Vince Calhoun, and Junyoung Chung. Iterative refinement of the approximate posterior for directed belief networks. *Advances in Neural Information Processing Systems*, 29, 2016.
- [43] Rahul Krishnan, Dawen Liang, and Matthew Hoffman. On the challenges of learning with inference networks on sparse, high-dimensional data. In *International Conference on Artificial Intelligence and Statistics*, pages 143–151. PMLR, 2018.
- [44] Joe Marino, Yisong Yue, and Stephan Mandt. Iterative amortized inference. In *International Conference on Machine Learning*, pages 3403–3412. PMLR, 2018.
- [45] D Goodsell. PDB-101 Molecule of the Month: Hsp90. 2008.
- [46] Clemens Plaschka, Pei-Chun Lin, and Kiyoshi Nagai. Structure of a pre-catalytic spliceosome. *Nature*, 546(7660):617–621, 2017.

- [47] Alexandra C Walls, Young-Jun Park, M Alejandra Tortorici, Abigail Wall, Andrew T McGuire, and David Veesler. Structure, function, and antigenicity of the SARS-CoV-2 spike glycoprotein. *Cell*, 181(2):281–292, 2020.
- [48] Wilson Wong, Xiao-chen Bai, Alan Brown, Israel S Fernandez, Eric Hanssen, Melanie Condron, Yan Hong Tan, Jake Baum, and Sjors HW Scheres. Cryo-EM structure of the Plasmodium falciparum 80S ribosome bound to the anti-protozoan drug emetine. *Elife*, 3:e03080, 2014.
- [49] Diederik P Kingma and Jimmy Ba. Adam: A method for stochastic optimization. *arXiv preprint arXiv:1412.6980*, 2014.
- [50] Adam Paszke, Sam Gross, Francisco Massa, Adam Lerer, James Bradbury, Gregory Chanan, Trevor Killeen, Zeming Lin, Natalia Gimelshein, Luca Antiga, et al. Pytorch: An imperative style, high-performance deep learning library. *Advances in Neural Information Processing Systems*, 32, 2019.
- [51] Thomas D Goddard, Conrad C Huang, Elaine C Meng, Eric F Pettersen, Gregory S Couch, John H Morris, and Thomas E Ferrin. UCSF ChimeraX: Meeting modern challenges in visualization and analysis. *Protein Science*, 27(1):14–25, 2018.
- [52] Marin Van Heel and Michael Schatz. Fourier shell correlation threshold criteria. *Journal of Structural Biology*, 151(3):250–262, 2005.
- [53] Krzysztof M Gorski, Eric Hivon, Anthony J Banday, Benjamin D Wandelt, Frode K Hansen, Mstvos Reinecke, and Matthias Bartelmann. HEALPix: A framework for high-resolution discretization and fast analysis of data distributed on the sphere. *The Astrophysical Journal*, 622(2):759, 2005.
- [54] Adam Paszke, Sam Gross, Soumith Chintala, Gregory Chanan, Edward Yang, Zachary DeVito, Zeming Lin, Alban Desmaison, Luca Antiga, and Adam Lerer. Automatic differentiation in pytorch. 2017.
- [55] Julian Panetta. Optimizing over SO(3). Technical report, University of California, Davis, 2018.
- [56] F Sebastian Grassia. Practical parameterization of rotations using the exponential map. *Journal of Graphics Tools*, 3(3):29–48, 1998.

Supplementary Material

Improving Ab-Initio Cryo-EM Reconstruction with Semi-Amortized Pose Inference

A Pose Optimization with SGD

During the auto-decoding stage, we alternate between five iterations of pose updates and one iteration of volume update. To update poses, we keep the volume fixed and optimize for the negative log-likelihood (Eq. 3) with respect to the pose parameters. We define the new pose estimate based on the current one as follows:

$$R_{t+1} = R_\delta R_t \quad (10)$$

where R_δ is an infinitesimal rotation matrix perturbing the current estimate. We select axis-angle representation to parameterize this perturbation matrix R_δ . By a single vector $\omega \in \mathbb{R}^3$, one can represent both the axis $\|\omega\|$ and the angle $0 < \frac{\omega}{\|\omega\|} < \pi$ for any given rotation. Using Rodrigues formula, the perturbation matrix $R_\delta(\omega)$ can be parameterized as a function of ω . To find the optimal ω , one can initialize it with zero vector, and then use automatic differentiation [54] in pytorch to compute the gradient with respect to ω and make updates using Adam [49]. However, a naive implementation of the function $R_\delta(\omega)$ would lead to numerically unstable calculations of the partial derivative $\frac{\partial R_\delta}{\partial \omega}$. In fact, there is a singularity at the zero vector, and the partial derivative involves terms that are unstable around the origin. Formally, the derivative of i -th column of the rotation matrix R_δ with respect to the vector ω is [55, 56],

$$\begin{aligned} \frac{\partial R_\delta^{(i)}}{\partial \omega} = & - \left(\mathbf{e}^{(i)} \otimes \omega + [\mathbf{e}^{(i)}]_\times \right) \frac{\sin(\|\omega\|)}{\|\omega\|} + [(\omega \cdot \mathbf{e}^{(i)}) I + \omega \otimes \mathbf{e}^{(i)}] \left(\frac{1 - \cos(\|\omega\|)}{\|\omega\|^2} \right) \\ & + (\omega \otimes \omega) \left((\omega \cdot \mathbf{e}^{(i)}) \frac{2 \cos(\|\omega\|) - 2 + \|\omega\| \sin(\|\omega\|)}{\|\omega\|^4} \right) \\ & + [(\omega \times \mathbf{e}^{(i)}) \otimes \omega] \frac{\|\omega\| \cos(\|\omega\|) - \sin(\|\omega\|)}{\|\omega\|^3}. \end{aligned}$$

where \otimes and \times are tensor and cross products, respectively. $\mathbf{e}^{(i)}$ is the i -th standard basis in 3D and $[\mathbf{v}]_\times$ denotes the cross product matrix for the vector \mathbf{v} . In all four terms, there are scalars such as $\frac{\sin(\|\omega\|)}{\|\omega\|}$ or $\frac{1 - \cos(\|\omega\|)}{\|\omega\|^2}$ that evaluate to $\frac{0}{0}$ at zero angle $\omega = 0$. Similar to [55], for $\|\omega\| \ll 1$, we substitute these terms with their numerically robust Taylor expansion, for instance,

$$\begin{aligned} \frac{\sin(\|\omega\|)}{\|\omega\|} &= 1 - \frac{\|\omega\|^2}{6} + O(\|\omega\|^4), \\ \frac{1 - \cos(\|\omega\|)}{\|\omega\|^2} &= \frac{1}{2} - \frac{\|\omega\|^2}{24} + O(\|\omega\|^4). \end{aligned}$$

We implement a differentiable and numerically stable version of the function $R_\delta(\omega)$ in pytorch and use it in our pose estimation module.

B Specialization of Encoder Heads

A natural question about the multi-head encoder is: how each head does take part in pose encoding process? To address this, using the synthetic datasets, we conduct an experiment with our multi-head architecture ($M = 4$) and visualize the performance of each head on different regions of $SO(3)$ space. In particular, as before, we define a uniform grid on the unit sphere using HEALPix [53] and assign images to their corresponding cells based on the view-direction. Now, for all images end up in the same cell, we compute the average rotation error and visualize it separately for each head. As shown in Fig. 6, all heads actively participate in pose estimation and they are able to specialize in prediction of poses for images with certain view-direction. A similar result has been provided in prior work on MCL [27, 13], to show that minimizing the error made by the best prediction (“oracle” loss) encourages diversity in deep ensembles. In our problem, by optimizing a “winner-takes-all” loss, the whole burden of pose estimation is no longer on a single network but it gets divided between multiple heads as separate predictors.

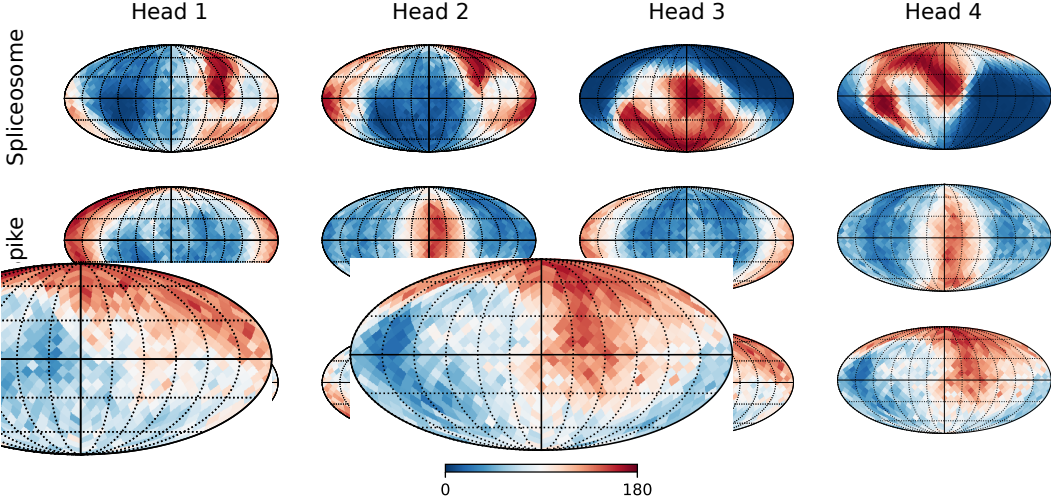


Figure 6: Average rotation error visualized over the unit sphere for different heads of our multi-head pose encoder ($M = 4$). The sphere is uniformly divided into cells using HEALPix [53] and based on their ground-truth view-direction, images are assigned to corresponding cells. For each cell, the average rotation error is visualized, showing diverse behavior of different heads across the space. Blue and red colors show low and high error regions, respectively. Error ranges from zero to 180 degrees.

C More on Semi-Amortized vs. Fully-Amortized

To validate the advantages of direct pose optimization in our semi-amortized method, we further show more qualitative examples of paths taken by pose estimates over the optimization landscape during reconstruction in Fig. 7. For both methods, optimization start from the same point marked by **black** dot in the vicinity of the distribution mode. It will then continue in paths colored in **blue** and **red** for semi-amortized and full-amortized methods, respectively. We observe in all examples that iterative updates by stochastic gradient descent demonstrate a stable convergence toward the optima while poses obtained by amortized inference show unstable behavior around the mode.

D More on Multi-Modal Pose Posterior

Through more examples (Fig. 8), we demonstrate that cryoAI fails to handle ambiguity in pose estimation on HSP dataset. The visualization shows that pose estimates by cryoAI become stuck in incorrect modes whereas our pose encoder with multi-head architecture is able to return a pose candidate that captures the correct mode.

E Videos

In the supplementary package, using ChimeraX [51] we provide videos that show reconstructions obtained by semi-amortized method, cryoAI and cryoSPARC on all synthetic and experimental datasets. In these 3D visualizations, we rotate the structure to show the resolved structure from different views.

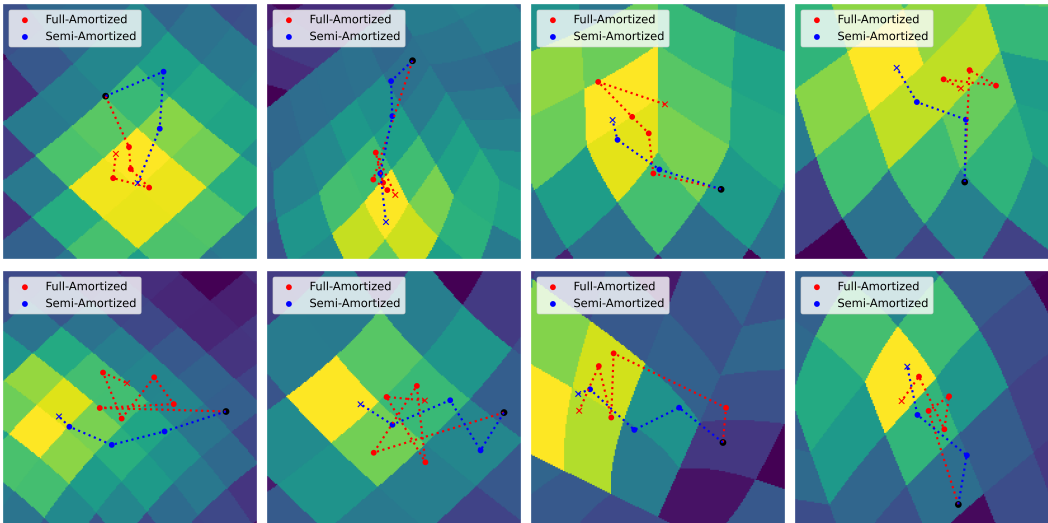


Figure 7: Using four examples per dataset, the behavior of fully-amortized and semi-amortized pose inference methods are compared. Two rows correspond to Spliceosome and Spike datasets, respectively. Each plot shows the approximate log pose posterior, marginalized over in-plane rotations represented as a heat map on a uniform grid over the unit sphere S^2 . Gnomonic projection to 2D is also applied, followed by zooming on the proximity of the mode of interest. **Black** dot is the starting point while **blue** dots and **red** dots show poses estimated by fully- and semi-amortized methods, respectively.

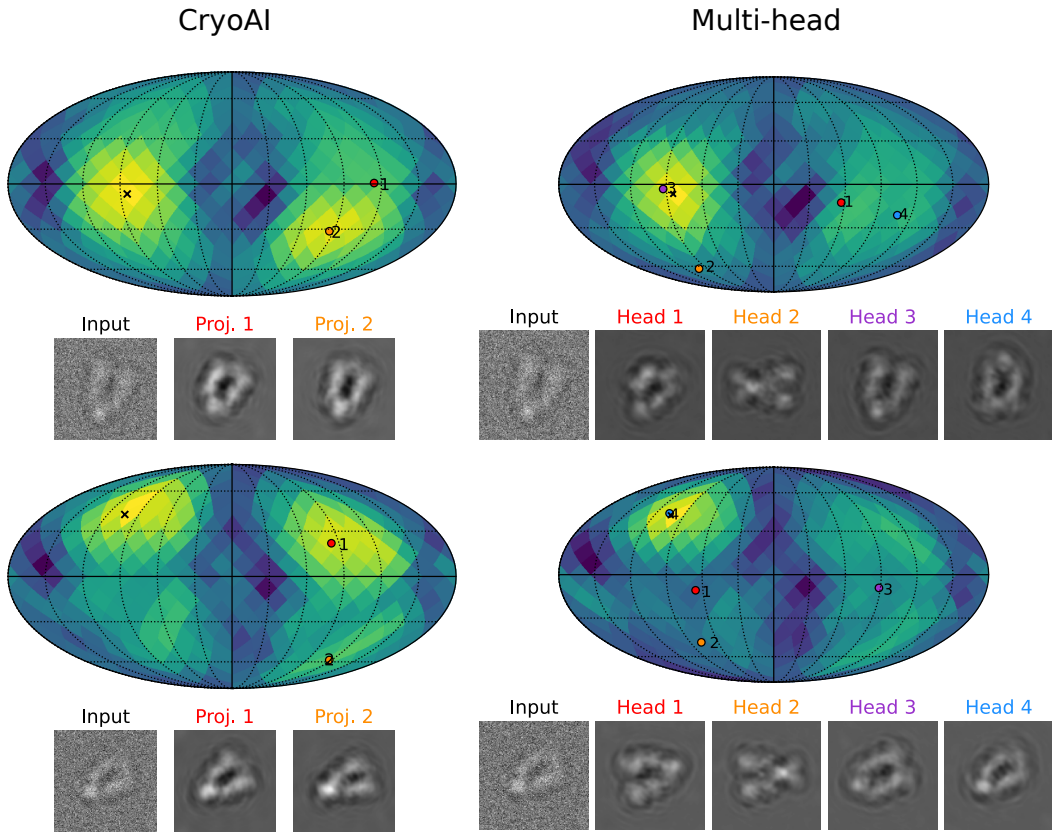


Figure 8: The approximate log posterior of view-direction visualized on the unit sphere with highlighted areas showing modes of the distribution. CryoAI [10] and our multi-head encoders provide two and four pose estimates, respectively, which are marked with colored dots on the sphere (the order of poses is arbitrary). The corresponding projections are also illustrated. CryoAI cannot identify the correct mode of pose distribution.